Copper-Doped Platinum/Metal-Organic Framework Nanostructures for Imaging Guided Photothermal and H_2O_2 Self-Supplying Photodynamic/Photothermal/Chemodynamic Therapy

Jiuhai Wang[a]*, Yutian Gu[a], Yadi Fan[a], Mo Yang[a]*

[a] Department of Biomedical Engineering, The Hong Kong Polytechnic University, Hong Kong S. A. R. China

* Corresponding authors:
Jiuhai Wang - 16903649r@connect.polyu.hk;
Mo Yang - mo.yang@polyu.edu.hk;

Keywords: Metal-organic frameworks (MOFs); Cancer therapy; Combinational phototherapy; Photothermal therapy; Chemodynamic therapy.

Abstract

Simultaneous photodynamic/photothermal therapy (PDT/PTT) is a combination cancer treatment that combines the principles of both PDT and PTT to achieve an effective and comprehensive attack on cancer cells. However, both two approaches require an external light source to generate reactive oxygen species (ROS) and thermal heat, which could potentially hinder therapeutic efficacy due to the low tissue penetration of light in vivo. Chemodynamic therapy (CDT) is a type of therapy that uses ROS generated by a chemical reaction between a prodrug and a catalyst to kill cancer cells. We developed a combination therapy of three modalities PTT/PDT/CDT using metal-organic framework (MOFs). The Cu^{2+} -doped MOF PCN-224 nanostructures modified with Platinum (Pt) cluster and folic acid (FA) provided excellent tumor targeting, photothermal conversion ability, ROS generated by Pt cluster and Cu^{2+} under 650 nm light irradiation. Moreover, this multi-model nanocomposite had extremely low dark toxicity, while excellent phototoxicity under the combination laser irradiation 650 nm, both *in vitro* and *in vivo*. Therefore, our prepared folic acid conjugated PCN-224/Pt/Cu^{2+} (FA-PPC) nanosphere could be applied as a very promising multi-modal phototherapeutic agent for enhanced cancer therapy in future clinical applications.

1. INTRODUCTION

Emerging cancer treatments such as photothermal therapy (PTT), photodynamic therapy (PDT), and chemodynamic therapy (CDT) have advanced cancer therapy in recent years.[1–5] Near-infrared (NIR) light-mediated photothermal therapy converts light energy into hyperthermia, resulting in the thermal ablation of adjacent cells. PTT has become a promising alternative treatment for many diseases owing to their unique advantages, including improved selectivity, minimal invasiveness and side effects.[6–8]

In addition, ROS such as hydrogen peroxide (H_2O_2), singlet oxygen ($^1O_2$), and hydroxyl radical (•OH) are capable of killing cancer cells by damaging nucleic acids and proteins intracellularly.[9] Photodynamic therapy induces cell apoptosis by cytotoxic $^1O_2$ produced by photosensitizer under light irradiation.[5,10–13] Although PDT has been widely investigated for cancer treatment, its efficacy remains unsatisfactory due to the nature of hypoxia environment in cancer cells. Low level of dissolved intracellular oxygen hinders the production of $^1O_2$ even in the presence of highly photosensitive catalysts such as chlorin e6 (Ce6),[14,15] indocyanine green (ICG)[16] and nanoparticle modulators including quantum dots (QDs),[17] upconversion nanoparticles,[18] gold nanocages,[19] *etc*. Compared with the strategy of delivering exogenous oxygen into cells, one easier and more feasible way to relieve hypoxia condition is to convert H_2O_2 into O_2. Despite low intracellular oxygen level, many types of tumor cells have higher intracellular H_2O_2 level compared with normal cells, which suggests a great potential of a constant supply of O_2 from H_2O_2 decomposition.

Moreover, the excess H_2O_2 accumulates in cancer cells could also be the substrate of Fenton reaction for CDT.[20] Chemodynamic therapy employs iron-mediated Fenton-type reactions to induce intracellular oxidative stress by converting less-reactive endogenous H_2O_2 into •OH, the more reactive and toxic ROS.[21–23] Such a unique reaction and •OH generation approach will enable CDT to circumvent the major inherent obstacles of hypoxia-associated resistance

of tumor therapy.[24–26] However, intracellular glutathione (GSH) impedes PDT and CDT efficacy due to inherent cellular antioxidant defense system. While several studies have utilized inorganic nanoparticles (NPs) CuO, MnO as nanoenzymes to stimulate Fenton-like reaction and produce •OH, few of them have reported a reliable delivery approach into cells and a controlled release of the metal ions after internalization by target cells.[27–30]

Inspired by high expression of H_2O_2 nature of cancer cells and photosensitizer potential of porphyrinic MOFs,[4,10,31–34] here we present a smart "all-in-one" nanoplatform with a strategy of combining PTT/PDT/CDT in one single nanoprobe copper- doped platinum nanocrystal-coated metal-organic framework PCN-224 (PPC). This activating hybrid nanoparticle benefits from 1) photothermal effect of platinum nanocluster, 2) photodynamic nature of PCN-224 under NIR light, 3) •OH production by Fenton-like copper ion. We utilized a layer-by-layer synthesis approach to fabricate a PCN-224 core through a solvothermal method, following by coating with a layer of Pt nanocrystals on the MOF surface, then doping Cu^{2+} into the PCN-224-Pt hybrid structure. Finally, folic acid was conjugated onto the nanoplatform in order to specifically target the breast cancer cells without harming normal tissue. Intracellular GSH-assisted Cu^{2+} release and reduction to Cu^{+} triggered the Fenton catalytic activity for enhanced CDT due to the GSH depletion, while an enhanced photodynamic efficacy was achieved in a hypoxia-relieved environment by self-supplying H_2O_2 and GSH depletion. Meanwhile, Pt nanocrystals can not only activate O_2 to $^1O_2$ but also provide photothermal effect under light irradiation. Therefore, the integration of Pt nanocrystals with semiconductor-like porphyrinic MOFs and Cu^{2+} doping could achieve synergistic therapeutic effects on tumor cells.[35] With FA conjugation to PPC MOF (FA-PPC), this nanoplatform can simultaneously enable hydroxyl radical generation, hypoxia relief and GSH depletion, leading to a targeted enhanced CDT/PDT/PTT triple-modality antitumor therapy under the guidance fluorescence imaging.

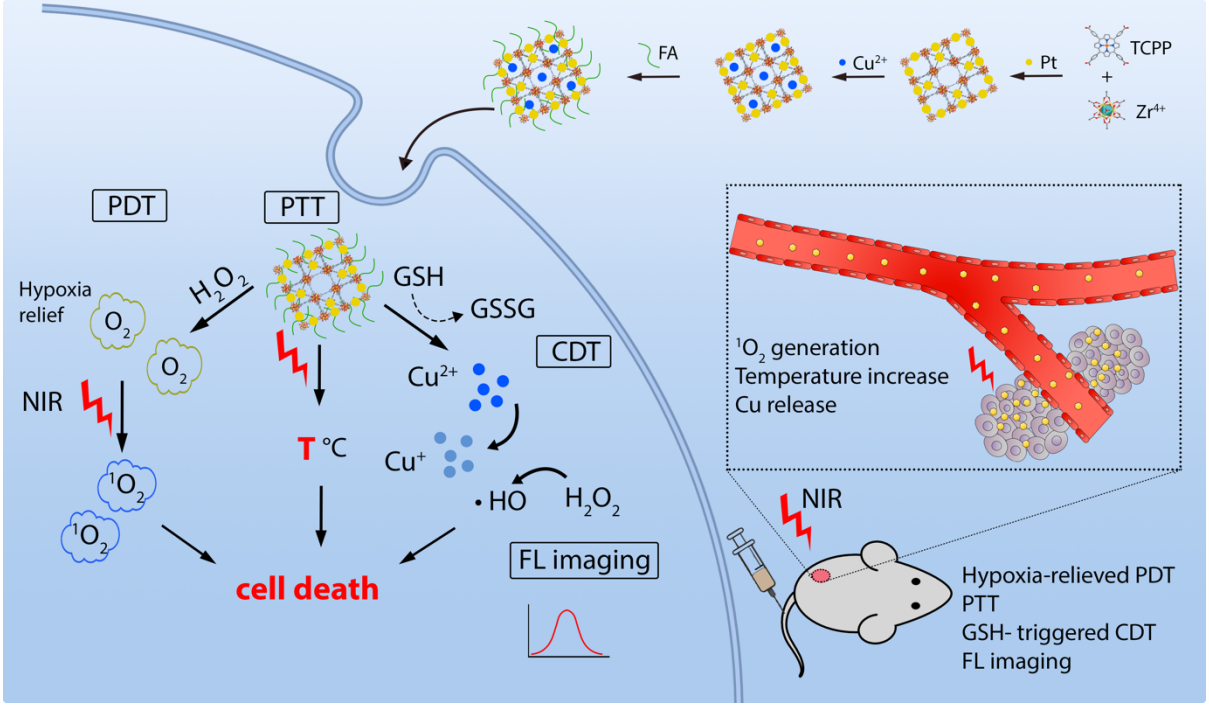

Figure 1. Schematic illustration of layer-by-layer synthesis of smart FA-PPC nanoparticles and mechanism of imaging-guided photothermal and H_2O_2 self-supplying photodynamic/chemodynamic therapy.

2. EXPERIMENTAL SECTION

2.1 Preparation of PCN-224 Nanoparticles

FA-PPC was obtained through a layer-by-layer synthesis method reported previously. The PCN-224 was synthesized using a solvothermal approach described previously. The detailed synthesis methodology can be found in our previous publications.[11,31]

2.2 Preparation of PCN-224-Pt

PCN-224 NPs were resuspended in 2.5 mL of ethylene glycol (EG) and preheated at 120 °C for 10 min. Pt nanoclusters were synthesized onto the PCN-224 NPs according to the methodology described in previous study.[31]

2.3 Preparation of PCN-Pt-Cu (PPC)

Copper chloride (Sigma-Aldrich, 0.1 M) was added dropwise into PCN-Pt nanocomposite in 8.3% acetic acid (TCI Chemicals) solution under constant vigorous stirring at room temperature for another 48 hours to allow copper to be incorporated into the center of porphyrin. The resulting product was washed three times with water.

2.4 Pt-mediated O_2 Generation

PPC nanocomposite was dispersed in water under vigorous stirring. H_2O_2 was then added to the solution. We monitored the oxygen concentration of the solution using a portable dissolved oxygen meter.

2.5 Extracellular $^1O_2$ Measurement

Singlet Oxygen Sensor Green (SOSG) kit was obtained from ThermoFisher Scientific. 10 μg/mL SOSG was mixed with PPC sample (200 μg/mL, 1 mL) under light (650 nm, 0.6 W/cm^2) for 5 min. Fluorescence spectrum was recorded under excitation of 395 nm with one minute interval. DPBF (Sigma-Aldrich) solution that dissolved in 1 mM DMSO was added to the solution (200 μg/mL, 1 mL) under light (650 nm, 0.6 W/cm^2) for 5 min. The DPBF absorbance at 414 nm was recorded at appointed times.

2.6 GSH-mediated Cu Release

PPC nanocomposite was added to a series of concentrations of GSH water solution under stirring. The solution was then centrifugated and supernatant was collected for measurement of inductively coupled plasma optical emission spectrometry (ICP-OES, Agilent).

2.7 Cellular Uptake of PPC Nanocomposite

MCF-7, A549 cells were plated at a density of 1×10^5 cells and cultured for 24 hours. Cell culture methods were adopted from ATCC. 200 μg/mL PPC was added to the cells in cell culture medium and incubated with cells for another 4 hours. The cells were then triple washed by PBS before analyzed by confocal microscopy imaging and flow cytometry.

2.8 Intracellular Hypoxia Relief

MCF-7 cells were plated in five 10-mm dishes at a density of 1×10^4 cells/cm^2. One dish was maintained in normoxia incubator, while the other four dishes treated with PBS, PCN-224, PCN-Pt, and PPC were incubated in a hypoxia incubator with 5% O_2, and 5% CO_2. After 4 hours, the cells were then stained with Image-iT™ Red Hypoxia Reagent for 1 h (5 μM,

Invitrogen™). Confocal microscopy images were obtained using Leica TCS SPE microscope with confocal laser.

2.9 Intracellular ROS generation

MCF-7 cells (ATCC, USA) were plated in five 10-mm dishes at a density of 1×10^4 cells/cm^2. The cells were treated with PBS, PCN-224, PCN-Pt, PPC under 650 nm laser irradiation for 5 min (0.6 W/cm^2). Then, the cells were incubated with SOSG and DCF-DA reagents for 30 min at 37 °C. Confocal microscopy images were obtained using Leica TCS SPE microscope.

2.10 Tissue penetration in Tumor Organoids

Breast cancer organoids were generated by seeding 3,000 MCF-7 cells in U-bottom Nunc 96-well culture plate (ThermoFisher Scientific) and grew for 3-4 days. Once the organoids were formed, FA-PPC nanocomposites were added to the cells and co-cultured in plates for 4 hours. The tumor organoids were placed in a new plate then washed three times with PBS. The tumor organoids were imaged using confocal microscopy with 3D scanning.

2.11 Animal study

All the mice were purchased from The Hong Kong Polytechnic University Animal Facility. All animal procedures were performed following the protocols approved by the Animal (CONTROL OF EXPERIMENT) Regulations of The Hong Kong Polytechnic University.

2.12 In vivo synergistic PDT/PTT/CDT therapy

In the in vivo study, thirty tumor-bearing mice were grouped into five groups with six mice in each group. The mice were intravenously administered with 1) saline, 2) PCN-224 + 650 nm laser, 3) PCN-Pt + 650 nm laser, 4) PPC + 650 nm laser, 5) FA-PPC + 650 nm laser. The nanoparticle concentration of each group was 200 μg/mL, and the power of laser irradiation was 0.6 W/cm^2. The tumor dimensions (length by width) and body weight were measured daily over 9 days post-treatment. The mice were sacrificed on day 10, the tumors and organs

were collected. The major organs of the five groups were dissected to make paraffin sections for further H&E staining.

3. RESULTS AND DISCUSSION

3.1 Synthesis and characterization of the FA-PCN-224/Pt/Cu hybrid nanoparticle

The hybrid PCN-Pt-Cu (PPC) with an average diameter of 190 nm were synthesized using a layer-by-layer approach as illustrated in Figure 1. PCN-224 MOF as a template was first synthesized through a solvothermal reaction at 120 °C as described in previous reports. Platinum nanocrystals were formed on the surface of PCN-224 by reacting $H_2PtCl_6 \cdot 6H_2O$ in ethylene glycol/H_2O solution in the presence of PVP at 120 °C under vigorous stirring. Transmission electron microscopy (TEM) image in Figure 2A showed a cubic morphology of PCN-224 decorated with small Pt nanocrystals (less than 5 nm). The magnified image showed Pt nanocrystals adhering to the surface of MOF PCN-224. Elemental mapping uniform distributions of Zr element in MOF and Pt element in Pt nanocrystals, indicating the successful coating of Pt nanocrystals on the Zr-based MOFs. Figure 2B indicates the relative UV-visible absorbance of PPC increased markedly between the wavelength of 450 - 700 nm compared to bare PCN-224, indicating the potential of being used as a NIR photosensitizer for PDT of tumor. X-ray diffraction (XRD) pattern in Figure 2C confirmed the pattern of as-synthesized PCN-224 and PCN-Pt, and PPC measured with 2θ steps of 0.02° matched the simulated PCN-224 and Pt standard curve. The crystal plane [112], [022], [222] of Zr, and [111], [200] of Pt indicated by the arrow showed the presence of Zr-MOF and Pt nanocrystals in the nanoparticle composite. PPC could be well-dispersed in water with a mean hydrodynamic diameter of ∼190 nm as shown in Figure 2D. The air bubbles were visually observable when H_2O_2 was added to the PPC nanocomposite, and the rapid increase of real-time O_2 concentration demonstrated the catalytic effect of PPC nanoparticles on H_2O_2 decomposition. This result encouraged us to further explore its potential in intracellular

hypoxia relief for the tumor cells. X-ray photoelectron spectroscopy (XPS) spectrum of PPC nanocomposite reflected the presence of core metal components including Zr, Pt, and Cu. In addition, the high-resolution XPS spectrum of Cu_{2p} suggested that the Cu existed in the form of Cu^{2+} within the PPC nanocomposite. The data also revealed that the amount of Zr and Pt atom were 1.37% and 0.74%, with the amount of Cu doping being nearly 0.45%, suggesting a Cu-dope Zr MOF - Pt nanocomposite (Figure 2F-I).

3.2 Synergistic photodynamic, photothermal and chemodynamic capacity of PPC

An increasing number of photosensitizers have been reported to effectively generate $^1O_2$, with examples such as metal nanoparticles, indocyanine green, porphyrins, and their derivatives being widely studied.[36–38] The integration of the second-generation photosensitizer porphyrin into MOFs could bring additional advantages such as NIR-activated PDT, nanoscale porous structure with high drug loading capacity, enriched surface groups available for chemical conjugation, etc. Here, owing to porphyrin ligands in the nanocomposite, PPC exhibited strong ability of $^1O_2$ generation. Figure 3A shows that SOSG fluorescence spectra with an emission maximum at 535 nm was increased markedly after exposure of 650 nm laser for 5 min, which confirmed the $^1O_2$ generation by PPC. A similar 1,3-diphenylisobenzofuran (DPBF) degradation experiment was conducted to measure the $^1O_2$ generation. Figure 3B shows a significant downtrend of DPBF absorption peaks at 420 nm over 5 min 650 nm laser irradiation (0.6 W/cm^2) in the presence of PPC, indicating a remarkable NIR-mediated $^1O_2$ production ability.

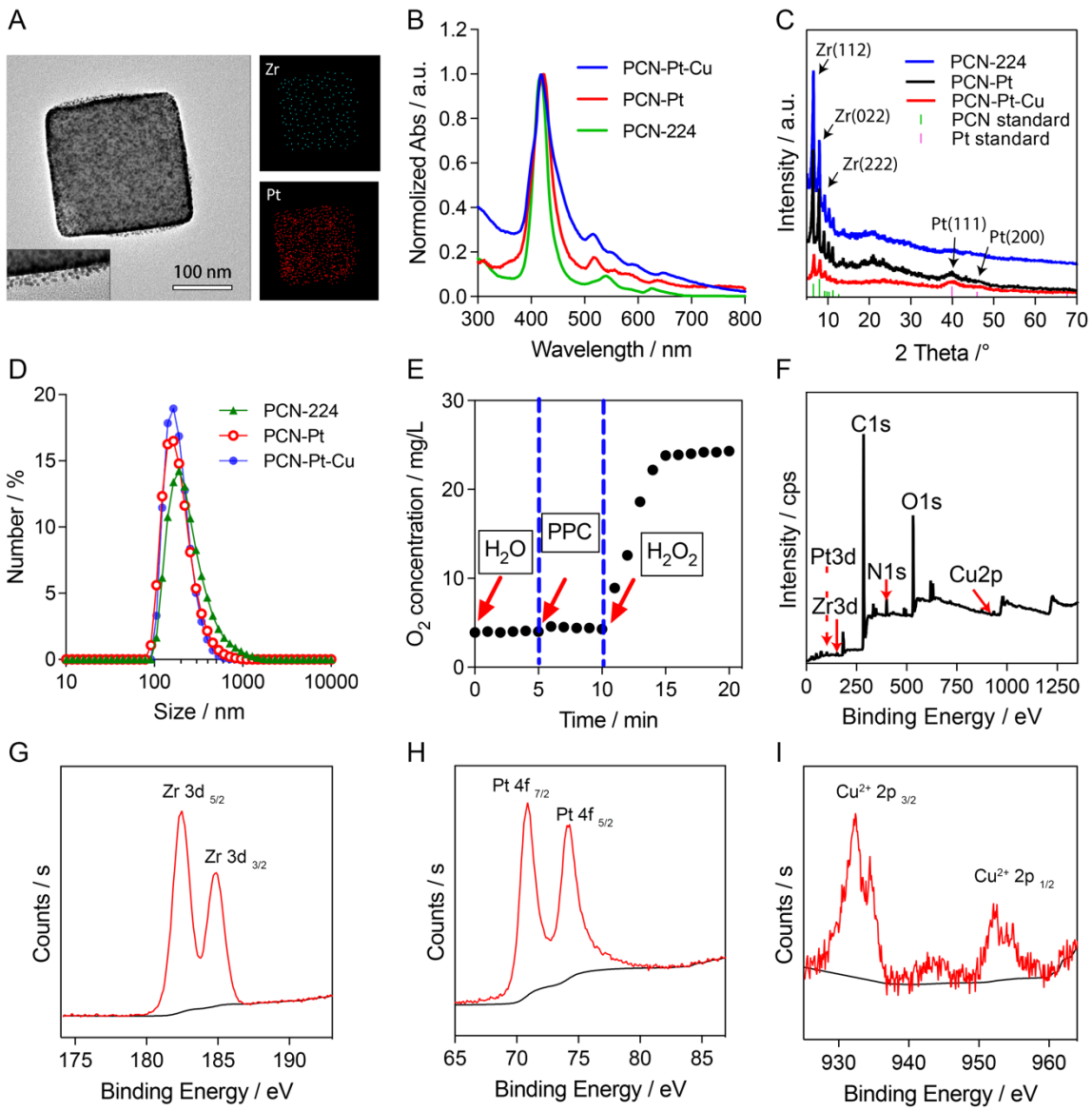

Figure 2. Characterizations of PPC MOF nanoparticles. (A) TEM image and elemental mapping of PPC. (B) Absorbance of PPC. (C) XRD of PPC. (D) DLS size distribution of PPC. (E) O2 generation by PPC. (F-I) XPS spectrum of PPC indicating the presence of Zr, Pt, and Cu.

Platinum nanomaterials display strong LSPR absorption from UV-visible range towards NIR, therefore could efficiently transfer the absorbed NIR optical energy into heat.[39] The photothermal efficacy of PPC nanocomposite was determined by a thermal camera under a 650 nm laser irradiation (0.6 W/cm^2). The temperature of 200 μg/mL PPC nanoparticles dispersed in PBS solution reached 42 °C after irradiated with 650 nm laser at power of 0.6 W/cm^2. A concentration-dependent photothermal effect was observed at various concentrations of PPC (Figure 3C).

GSH-triggered Cu^{2+} release and subsequent chemodynamic effect was further determined by electron spin resonance (ESR) measurement using 5,5-dimethyl-1-pyrroline-Noxide (DMPO) as •OH trapping agent. In the presence of GSH, PPC nanocomposite exhibited higher catalytic effect on DMPO, suggesting more •OH was produced from H_2O_2 by the PPC. By contrast, only a small amount of •OH was detected with absence of GSH, implying a mechanism of GSH-consumption based enhanced chemodynamic therapy (Figure 3D). GSH-triggered Cu^{2+} was also confirmed by inductively coupled plasma - optical emission spectrometry (ICP-OES). More than 20% of Cu^{2+} were released from the nanocomposite after 48 h in 1 mM GSH solution, whereas over 25% Cu^{2+} were released in 5 mM GSH solution after 48 h (Figure 3E). The Fenton-like Cu^{2+} in the presence of H_2O_2 showed good •OH production capability in methylene blue (MB) degradation assay. Notably, with low concentration of GSH (<1 mM), FA-PPC (0.2 mg/mL) showed remarkable •OH production capability. However, with higher concentration of GSH, almost no MB degradation was observed, indicating the scavenging effect of GSH toward •OH (Figure 3F). The Cu released from the FA-PPC NPs at neutral and acidic pH over 48 hours was measured by ICP-OES. Cu released significantly higher in acidic condition than that of in neutral condition (Figure S11).

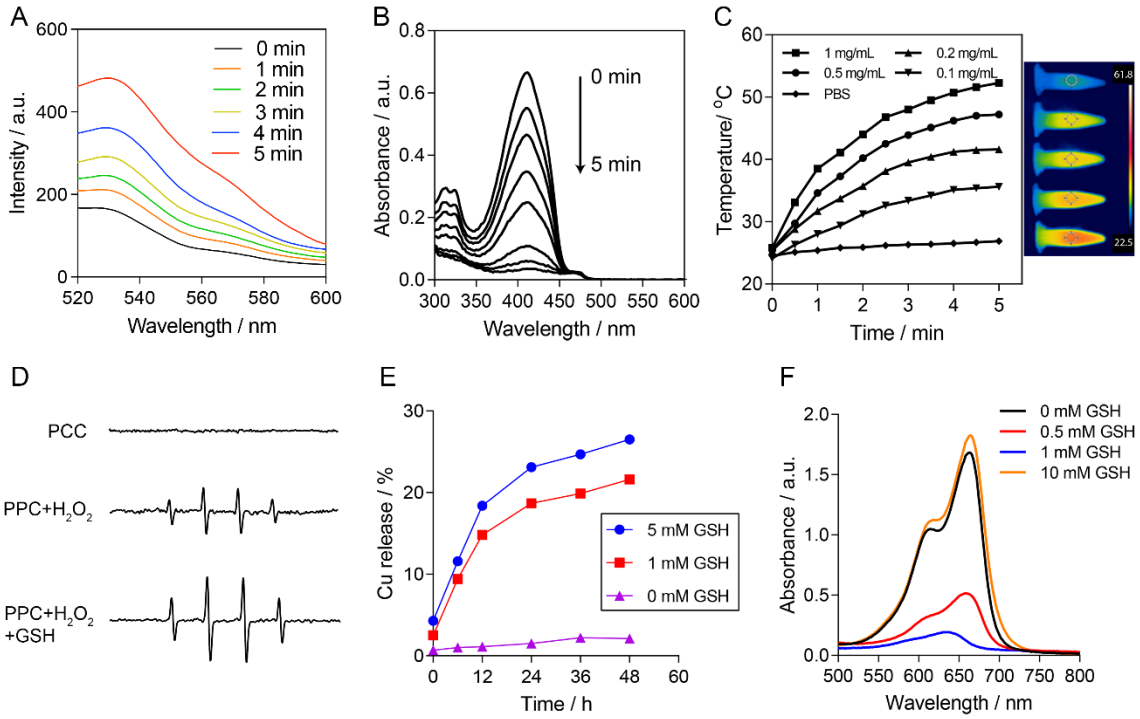

Figure 3. (A) SOSG fluorescence emission spectra in FA-PPC solution after exposure of 650 nm laser (0.6 W/cm^2) measured using fluorescence spectrometer. (B) ROS generation of PPC measured by DPBF probe under 650 nm laser irradiation (0.6 W/cm^2). (C) Concentration- dependent photothermal effect of FA-PPC. (D) ESR spectra of GSH-activated PPC reacting with H2O2 using DMPO as spin trap. (E) GSH assisted Cu^{2+} release in vitro measured by ICP. (F) MB degradation by •OH generated by FA-PPC (0.2 mg/mL) treated with different concentrations of GSH.

3.3 In vitro therapeutic effect of FA-PPC in breast cancer cells

The homotypic targeting ability of FA-conjugated PPC toward breast cancer MCF-7 cells was investigated using folate receptor- negative human non-small cell lung cancer cells (A549) as a control. Confocal microscopy and flow cytometry showed folate receptor-targeted FA-PPC nanocomposites preferentially accumulated in MCF-7 cells than in A549 cells (Figure 4A), owing to the high affinity of FA-PPC to the receptor on the MCF-7 membrane. The rapid proliferation of tumors outgrows their surrounding vasculature, resulting in a drop of normal oxygen levels of 2–9% to hypoxic levels of less than 2%. The Pt nanocrystals in the PPC nanocomposite can generate O_2 in tumor cells by catalyzing H_2O_2 into O_2 in cancer cells. The hypoxia probes react with intracellular O_2 and emit green fluorescence. Confocal microscopy showed weakened fluorescence emission in MCF-7 cells for both PCN-Pt and PPC nanocomposite treatment, indicating Pt nanocrystals were responsible for lifting hypoxic condition by producing O_2 comparing with PCN-224 alone

and PBS (Figure 4B). The PPC-mediated intracellular ROS generation was determined by 2,7-dichlorofluorescin diacetate (DCF-DA), which can be oxidized into 2′,7′-dichlorofluorescein (DCF) upon oxidation by ROS. However, since SOSG only reacts with intracellular $^1O_2$, the SOSG staining showed PCN-Pt nanocomposite produced significant more $^1O_2$ compared with PCN-224 alone as Pt converted H_2O_2 into O_2 to relieve hypoxia in the cells (Figure 4C). Both DCF-DA and SOSG staining were quantitatively measured on a microplate reader. PPC nanocomposite produced significantly more ROS than PCN-Cu and PCN-224 alone, indicating that Pt-assisted O_2 production increased efficiency of $^1O_2$ generation for PDT, and an enhanced CDT by GSH-activated Cu^{2+} release (Figure 4D and E).

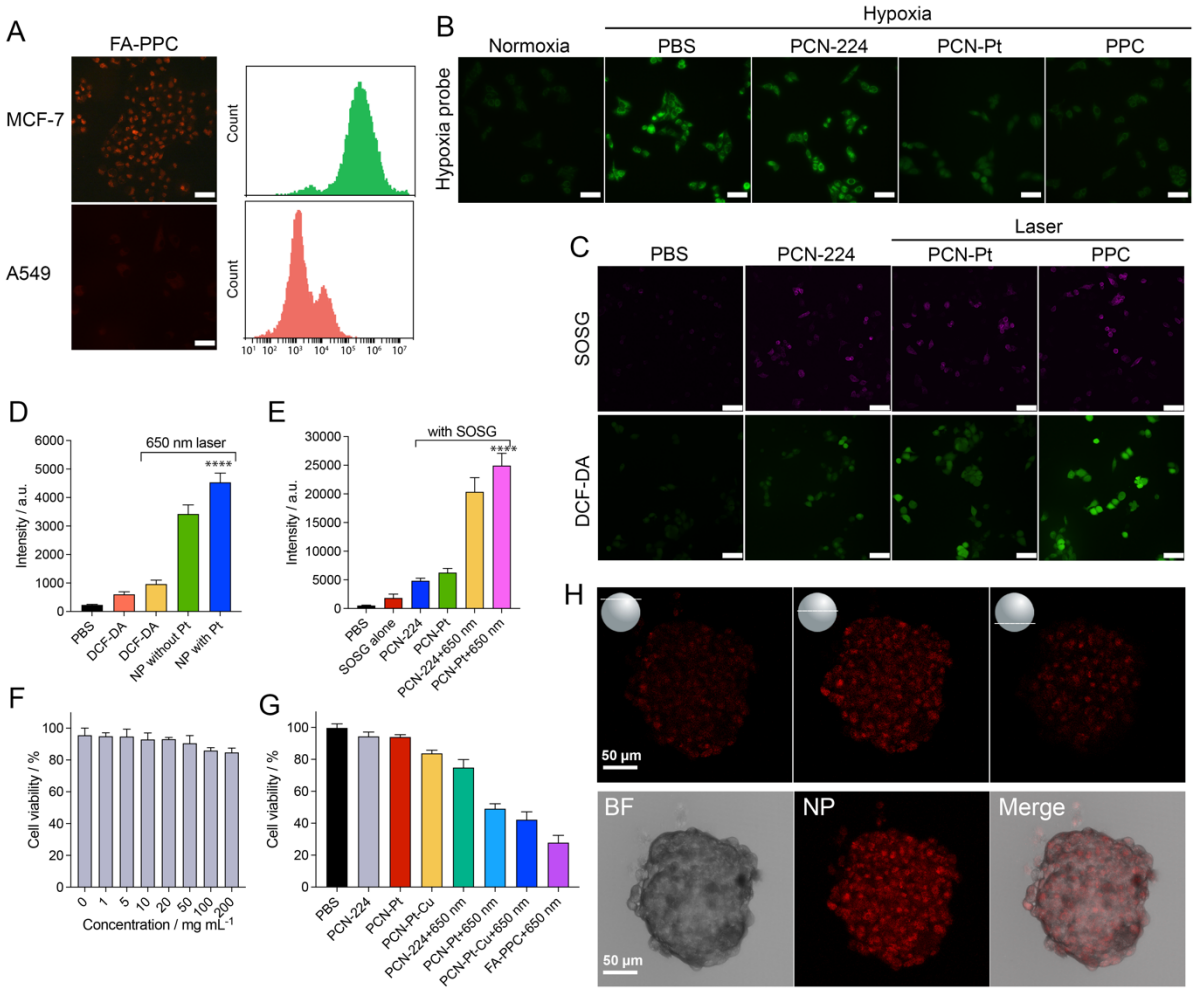

Figure 4 (A) FA-conjugated PPC specifically targets MCF-7 cells (Scale bar 25 μm). (B) Hypoxia relief by PPC in MCF-7 cells (Scale bar 25 μm). (C) imaging of SOSG and DCF-DA in MCF-7 cells and (D, E) quantitative fluorescent intensity of SOSG and DCF-DA in MCF-7 cells (Scale bar 25 μm). (F) Cell viability of HUVEC

cells treated with different concentrations of FA-PPC. (G) Cell viability of MCF-7 cells treated with different conditions of nanoprobes. (H) Tissue-penetrating capability of FA-PPC in tissue spheroid.

To determine the biocompatibility of FA-PPC, HUVEC cells were treated with different concentrations of FA-PPC nanocomposite. Cell viability of HUVEC was measured by CCK-8 assay. Notably, the cytotoxicity of FA-PPC nanocomposite remained low even at a concentration of 0.2 mg/mL, with a cell viability of over 82% after incubation with PPC for 24 h. Cancer therapeutic effect of FA-PPC nanocomposite was investigated by incubating MCF-7 with nanocomposite for 24 h followed by a localized 650 nm laser irradiation (0.6 W/cm^2). With the FA-PPC and 650 nm laser irradiation, we observed that more than 70% MCF-7 cells were killed, showing a higher therapeutic effect than other control groups such as non-targeted nanocomposite, non- Pt or Cu doped nanocomposite, and non-laser treated groups (Figure 4G). Furthermore, the intracellular GSH level were assessed using 5,5′-dithio-bis-2-nitrobenzoic acid (DTNB) assay. When the FA-PPC NPs were internalized into the cancer cells, GSH level decreased dramatically compared to the control group, suggesting an intracellular GSH depletion (Figure S12). We also investigated the cytotoxicity of FA-PPC NPs for normal cells HUVEC using CCK8 assay. At a NP concentration of 200 μg/ml, HUVEC cells remained a high viability (Figure S13). Many nanomedicines were reported to have satisfactory therapeutic effect against tumor cells, however, suffered from low tissue penetrating capability. Here, we demonstrated that FA-PPC nanocomposite with targeting moieties can penetrate tumor tissue and reach the center of the tumor. Confocal microscopy imaging allowed us to scan different planes along Z axis of the breast tumor organoids. We observed that more FA-PPC nanocomposites were accumulated in the center of the cancer organoids than those on the surface (Figure 4H). With combination of highly penetrative NIR laser irradiation, we anticipate that FA-PPC can achieve excellent cancer therapeutic effect in vivo.

3.4 Combinational anti-tumor effect in vivo

The potential hemolysis induced by nanoparticles is always a concern when applying nanomaterial for in vivo studies. The hemolysis assay results in Figure 5A showed negligible hemolysis of red blood cells after treatment of FA-PPC nanocomposite from 0 to 200 μg/mL, indicating a good hemocompatibility of FA-PPC. We then examined the accumulation of FA-PPC in the tumor site of mice using IVIS In Vivo Imaging System (Perkin Elmer). As shown in Figure 5B, remarkable fluorescence emission at the tumor site of MCF-7 bearing mouse model was observed 48 h post-intravenous injection, indicating an improved tumor targeting and accumulation ability, which could be attributed to FA conjugation on the PPC nanocomposite. Semi-quantitative analysis of NP uptake by tumor showed a similar trend as is shown in the IVIS images, consistent with the results of confocal imaging (Figure S15). In vivo temperature of tumor site was recorded by a FLIR thermal camera. Not surprisingly, FA-PPC induced highest temperature increase under 650 nm laser compared with other control groups where Pt was absent, demonstrating that photothermal effect was due to the Pt nanocrystals. Notably, PPC without targeting moiety FA also present a high temperature increase to 44 °C. It might be because non-targeted PPC diffused to tumor area due to the enhanced permeability and retention (EPR) effect. Thermal images showed that tumors from FA-PPC treated mice displayed a significantly higher temperature than those mice injected with saline after 5 min laser irradiation (0.6 W/cm^2).

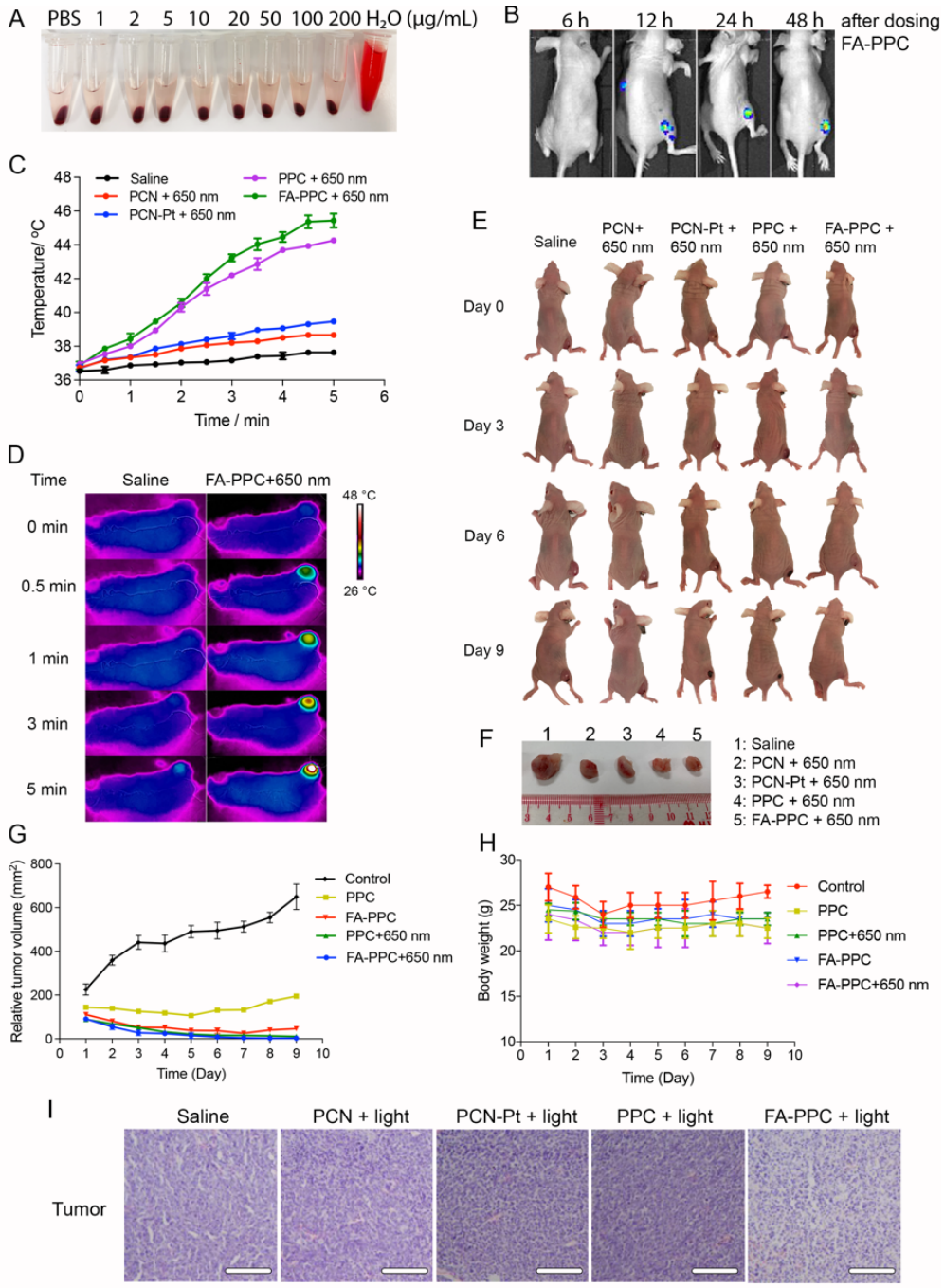

Figure 5 (A) Image of hemolysis of FA-PPC nanoparticles. (B) FA-PPC nanoparticles accumulated in mice tumor in IVIS images 48 h post-injection. (C) Temperature increases of different treatments in mice under 650 nm laser irradiation. (D) Thermal images of mice dosed with FA-PPC at concentration of 200 μg/mL. (E) Mice tumor growth of different treatments. Mice images captured at day 0, day 3, day 6, day 9. (F) Actual tumor size was determined after day 9. (G) Tumor volume of mice by different treatments of FA-PPC NPs. (H) Mice body wight was measured everyday over 9 days post-dosing of different NPs. (I) H&E staining of tumors 9-days after treatments.

The evaluation of anti-tumor efficacy in MCF-7 tumor-bearing mice were further carried out by intravenous administration of saline, PCN-224, PCN-Pt, PPC, FA-PPC into mice. The tumor sites were then exposed to 650 nm laser at a power of 0.6 W/cm^2 for 5 min. In contrast

to the rapid tumor growth of saline treated mice over 9 days post-injection, those mice treated with FA-PPC and 650 nm laser showed significant tumor inhibition (Figure 5E, F, and G). Moreover, the therapeutic groups of mice receiving i.v. injection of FA-PPC exhibited no apparent change in body weight during the 9 days of observation period (Figure 5H). Hematoxylin and eosin (H&E) staining showed a reduced tumor cells in the tumor tissue after the treatment of FA-PPC treated mice. By contrast, other groups did not show significant tumor cell death compared to the FA-PPC group (Figure 5I). In addition, H&E staining evidenced that there was no noticeable histological damage in the major organs of PBS, PCN-224 alone, PCN-Pt (PP), and FA-PPC treated mice (Figure S16). Biodistribution analysis of Zr in different organs including tumor by ICP-OES also revealed that the targeted NPs were accumulated in tumor tissue and no significant uptake were observed in other organs including heart, spleen and lung (Figure S17). The hematological indexes further supported that PPC NPs have no significant safety issues while circulating in the blood in mice (Figure S18). Therefore, the above results demonstrated that FA-PPC nanocomposite can be a localized therapeutic NP with synergistic therapeutic effect on tumor suppression.

4. CONCLUSION

In summary, an all-in-one copper-doped platinum/metal-organic framework FA-PPC nanostructure that enabled fluorescent imaging guided PDT, PTT and CDT therapy for breast cancer has been described. The self-suppling O_2 by Pt nanocrystals relieved hypoxia condition in tumor cells, allowing an enhanced PDT and PTT.[40,41] GSH-activated Cu^{2+} release and subsequent Fenton-type reaction produced •OH to disrupt lysosomal membrane, thereby triggered cell death of tumor to achieve high chemodynamic efficacy. Conjugation of folic acid endowed targeting effect therefore resulted in a high accumulation of the PPC nanocomposite

in breast tumor. This study could set an example for other nanomaterials being used for multi-modality therapeutic nanomedicines.

SUPPORTING INFORMATION

Additional supporting information, including electro microscopy characterizations of FA-PPC nanostructure, stability of FA-PPC, photothermal transduction efficiencies of FA-PPC, cytotoxicity analysis of FA-PPC, in vivo biosafety of FA-PPC.

AUTHOR INFORMATION

Corresponding Authors:

Jiuhai Wang – 16903649r@connect.polyu.hk;

Mo Yang - mo.yang@polyu.edu.hk;

ORCID

Jiuhai Wang: 0000-0003-3845-9901

Mo Yang: 0000-0002-3863-8187

CONFLICTS OF INTEREST

The authors declare no competing financial interests.

ACKNOWLEDGEMENTS

This work was supported by the Shenzhen Science and Technology Program-Basic Research Scheme (JCYJ20220531090808020), the Research Grants Council (RGC) of Hong Kong Collaborative Research Grant (C5078-21 EF), the Research Grants Council (RGC) of Hong Kong General Research Grant (PolyU 15217621 and PolyU 15216622), the Guangdong-Hong Kong Technology Cooperation Funding Scheme (GHP/032/20SZ and SGDX20201103095404018), the Hong Kong Polytechnic University Shenzhen Institute Bai

Cheng Bai Yuan Fund (I2022A002), and the Hong Kong Polytechnic University Internal Fund (1-ZVVQ, 1-CD6J and 1-CD8M).

REFERENCES

(1) Chen, J.; Glaus, C.; Laforest, R.; Zhang, Q.; Yang, M.; Gidding, M.; Welch, M. J.; Xia, Y. Gold Nanocages as Photothermal Transducers for Cancer Treatment. *Small* **2010**, *6* (7), 811–817. https://doi.org/10.1002/smll.200902216.

(2) Dolmans, D. E. J. G. J.; Fukumura, D.; Jain, R. K. Photodynamic Therapy for Cancer. *Nat. Rev. Cancer* **2003**, *3* (5), 380–387. https://doi.org/10.1038/nrc1071.

(3) Lin, L.; Wang, S.; Deng, H.; Yang, W.; Rao, L.; Tian, R.; Liu, Y.; Yu, G.; Zhou, Z.; Song, J.; Yang, H.-H.; Chen, Z.-Y.; Chen, X. Endogenous Labile Iron Pool-Mediated Free Radical Generation for Cancer Chemodynamic Therapy. *J. Am. Chem. Soc.* **2020**, *142* (36), 15320–15330. https://doi.org/10.1021/jacs.0c05604.

(4) Cheng, C.; Zhang, R.; Wang, J.; Zhang, Y.; Xiong, S.; Huang, Y.; Yang, M. Porphyrinic Metal–Organic Framework Nanorod-Based Dual-Modal Nanoprobe for Sensing and Bioimaging of Phosphate. *ACS Appl. Mater. Interfaces* **2020**, *12* (23), 26391–26398. https://doi.org/10.1021/acsami.0c06057.

(5) Wang, J.; Yang, M. 11 - Two-Dimensional Nanomaterials in Cancer Theranostics. In *Theranostic Bionanomaterials*; Cui, W., Zhao, X., Eds.; Micro and Nano Technologies; Elsevier, 2019; pp 263–288. https://doi.org/10.1016/B978-0-12-815341-3.00011-0.

(6) Zhang, Z.; Wang, J.; Chen, C. Near-Infrared Light-Mediated Nanoplatforms for Cancer Thermo-Chemotherapy and Optical Imaging. *Adv. Mater.* **2013**, *25* (28), 3869–3880. https://doi.org/10.1002/adma.201301890.

(7) Li, W.; Peng, J.; Tan, L.; Wu, J.; Shi, K.; Qu, Y.; Wei, X.; Qian, Z. Mild Photothermal Therapy/Photodynamic Therapy/Chemotherapy of Breast Cancer by Lyp-1 Modified Docetaxel/IR820 Co-Loaded Micelles. *Biomaterials* **2016**, *106*, 119–133. https://doi.org/10.1016/j.biomaterials.2016.08.016.

(8) Yong, Y.; Zhou, L.; Gu, Z.; Yan, L.; Tian, G.; Zheng, X.; Liu, X.; Zhang, X.; Shi, J.; Cong, W.; Yin, W.; Zhao, Y. WS2 Nanosheet as a New Photosensitizer Carrier for Combined Photodynamic and Photothermal Therapy of Cancer Cells. *Nanoscale* **2014**, *6* (17), 10394–10403. https://doi.org/10.1039/C4NR02453B.

(9) Ren, Z.; Sun, S.; Sun, R.; Cui, G.; Hong, L.; Rao, B.; Li, A.; Yu, Z.; Kan, Q.; Mao, Z. A Metal–Polyphenol-Coordinated Nanomedicine for Synergistic Cascade Cancer Chemotherapy and Chemodynamic Therapy. *Adv. Mater.* **2020**, *32* (6), 1906024. https://doi.org/10.1002/adma.201906024.

(10) Wang, J.; Fan, Y.; Tan, Y.; Zhao, X.; Zhang, Y.; Cheng, C.; Yang, M. Porphyrinic Metal–Organic Framework PCN-224 Nanoparticles for Near-Infrared-Induced Attenuation of Aggregation and Neurotoxicity of Alzheimer's Amyloid-β Peptide. *ACS Appl. Mater. Interfaces* **2018**, *10* (43), 36615–36621. https://doi.org/10.1021/acsami.8b15452.

(11) Wang, J.; Gu, Y.; Liu, X.; Fan, Y.; Zhang, Y.; Yi, C.; Cheng, C.; Yang, M. Near-Infrared Photothermally Enhanced Photo-Oxygenation for Inhibition of Amyloid-β Aggregation Based on RVG-Conjugated Porphyrinic Metal–Organic Framework and Indocyanine Green Nanoplatform. *Int. J. Mol. Sci.* **2022**, *23* (18), 10885. https://doi.org/10.3390/ijms231810885.

(12) Shen, J.; Yu, H.; Shu, Y.; Ma, M.; Chen, H. A Robust ROS Generation Strategy for Enhanced Chemodynamic/Photodynamic Therapy via H2O2/O2 Self-Supply and Ca2+ Overloading. *Adv. Funct. Mater.* **2021**, *31* (50), 2106106. https://doi.org/10.1002/adfm.202106106.

(13) Fu, L.-H.; Wan, Y.; Qi, C.; He, J.; Li, C.; Yang, C.; Xu, H.; Lin, J.; Huang, P. Nanocatalytic Theranostics with Glutathione Depletion and Enhanced Reactive Oxygen

Species Generation for Efficient Cancer Therapy. *Adv. Mater.* **2021**, *33* (7), 2006892. https://doi.org/10.1002/adma.202006892.
(14) Oushiki, D.; Kojima, H.; Terai, T.; Arita, M.; Hanaoka, K.; Urano, Y.; Nagano, T. Development and Application of a Near-Infrared Fluorescence Probe for Oxidative Stress Based on Differential Reactivity of Linked Cyanine Dyes. *J. Am. Chem. Soc.* **2010**, *132* (8), 2795–2801. https://doi.org/10.1021/ja910090v.
(15) Chin, W. W. L.; Heng, P. W. S.; Thong, P. S. P.; Bhuvaneswari, R.; Hirt, W.; Kuenzel, S.; Soo, K. C.; Olivo, M. Improved Formulation of Photosensitizer Chlorin E6 Polyvinylpyrrolidone for Fluorescence Diagnostic Imaging and Photodynamic Therapy of Human Cancer. *Eur. J. Pharm. Biopharm.* **2008**, *69* (3), 1083–1093. https://doi.org/10.1016/j.ejpb.2008.02.013.
(16) Barth, B. M.; I. Altinoğlu, E.; Shanmugavelandy, S. S.; Kaiser, J. M.; Crespo-Gonzalez, D.; DiVittore, N. A.; McGovern, C.; Goff, T. M.; Keasey, N. R.; Adair, J. H.; Loughran, T. P. Jr.; Claxton, D. F.; Kester, M. Targeted Indocyanine-Green-Loaded Calcium Phosphosilicate Nanoparticles for In Vivo Photodynamic Therapy of Leukemia. *ACS Nano* **2011**, *5* (7), 5325–5337. https://doi.org/10.1021/nn2005766.
(17) Jia, Q.; Ge, J.; Liu, W.; Zheng, X.; Chen, S.; Wen, Y.; Zhang, H.; Wang, P. A Magnetofluorescent Carbon Dot Assembly as an Acidic H2O2-Driven Oxygenerator to Regulate Tumor Hypoxia for Simultaneous Bimodal Imaging and Enhanced Photodynamic Therapy. *Adv. Mater.* **2018**, *30* (13), 1706090. https://doi.org/10.1002/adma.201706090.
(18) Idris, N. M.; Gnanasammandhan, M. K.; Zhang, J.; Ho, P. C.; Mahendran, R.; Zhang, Y. In Vivo Photodynamic Therapy Using Upconversion Nanoparticles as Remote-Controlled Nanotransducers. *Nat. Med.* **2012**, *18* (10), 1580–1585. https://doi.org/10.1038/nm.2933.
(19) Gao, L.; Liu, R.; Gao, F.; Wang, Y.; Jiang, X.; Gao, X. Plasmon-Mediated Generation of Reactive Oxygen Species from Near-Infrared Light Excited Gold Nanocages for Photodynamic Therapy in Vitro. *ACS Nano* **2014**, *8* (7), 7260–7271. https://doi.org/10.1021/nn502325j.
(20) Yang, N.; Xiao, W.; Song, X.; Wang, W.; Dong, X. Recent Advances in Tumor Microenvironment Hydrogen Peroxide-Responsive Materials for Cancer Photodynamic Therapy. *Nano-Micro Lett.* **2020**, *12* (1), 15. https://doi.org/10.1007/s40820-019-0347-0.
(21) Shi, Y.; Zhang, J.; Huang, H.; Cao, C.; Yin, J.; Xu, W.; Wang, W.; Song, X.; Zhang, Y.; Dong, X. Fe-Doped Polyoxometalate as Acid-Aggregated Nanoplatform for NIR-II Photothermal-Enhanced Chemodynamic Therapy. *Adv. Healthc. Mater.* **2020**, *9* (9), 2000005. https://doi.org/10.1002/adhm.202000005.
(22) Bai, S.; Yang, N.; Wang, X.; Gong, F.; Dong, Z.; Gong, Y.; Liu, Z.; Cheng, L. Ultrasmall Iron-Doped Titanium Oxide Nanodots for Enhanced Sonodynamic and Chemodynamic Cancer Therapy. *ACS Nano* **2020**, *14* (11), 15119–15130. https://doi.org/10.1021/acsnano.0c05235.
(23) Li, S.-L.; Jiang, P.; Jiang, F.-L.; Liu, Y. Recent Advances in Nanomaterial-Based Nanoplatforms for Chemodynamic Cancer Therapy. *Adv. Funct. Mater.* **2021**, *31* (22), 2100243. https://doi.org/10.1002/adfm.202100243.
(24) Liang, K.; Sun, H.; Yang, Z.; Yu, H.; Shen, J.; Wang, X.; Chen, H. Breaking the Redox Homeostasis: An Albumin-Based Multifunctional Nanoagent for GSH Depletion-Assisted Chemo-/Chemodynamic Combination Therapy. *Adv. Funct. Mater.* **2021**, *31* (22), 2100355. https://doi.org/10.1002/adfm.202100355.
(25) Liu, C.; Wang, D.; Zhang, S.; Cheng, Y.; Yang, F.; Xing, Y.; Xu, T.; Dong, H.; Zhang, X. Biodegradable Biomimic Copper/Manganese Silicate Nanospheres for

Chemodynamic/Photodynamic Synergistic Therapy with Simultaneous Glutathione Depletion and Hypoxia Relief. *ACS Nano* **2019**, *13* (4), 4267–4277. https://doi.org/10.1021/acsnano.8b09387.
(26) You, Q.; Zhang, K.; Liu, J.; Liu, C.; Wang, H.; Wang, M.; Ye, S.; Gao, H.; Lv, L.; Wang, C.; Zhu, L.; Yang, Y. Persistent Regulation of Tumor Hypoxia Microenvironment via a Bioinspired Pt-Based Oxygen Nanogenerator for Multimodal Imaging-Guided Synergistic Phototherapy. *Adv. Sci.* **2020**, *7* (17), 1903341. https://doi.org/10.1002/advs.201903341.
(27) Lin, X.; Liu, S.; Zhang, X.; Zhu, R.; Chen, S.; Chen, X.; Song, J.; Yang, H. An Ultrasound Activated Vesicle of Janus Au-MnO Nanoparticles for Promoted Tumor Penetration and Sono-Chemodynamic Therapy of Orthotopic Liver Cancer. *Angew. Chem.* **2020**, *132* (4), 1699–1705. https://doi.org/10.1002/ange.201912768.
(28) Lin, L.-S.; Song, J.; Song, L.; Ke, K.; Liu, Y.; Zhou, Z.; Shen, Z.; Li, J.; Yang, Z.; Tang, W.; Niu, G.; Yang, H.-H.; Chen, X. Simultaneous Fenton-like Ion Delivery and Glutathione Depletion by MnO2-Based Nanoagent to Enhance Chemodynamic Therapy. *Angew. Chem.* **2018**, *130* (18), 4996–5000. https://doi.org/10.1002/ange.201712027.
(29) Zhang, Y.; Wang, F.; Liu, C.; Wang, Z.; Kang, L.; Huang, Y.; Dong, K.; Ren, J.; Qu, X. Nanozyme Decorated Metal–Organic Frameworks for Enhanced Photodynamic Therapy. *ACS Nano* **2018**, *12* (1), 651–661. https://doi.org/10.1021/acsnano.7b07746.
(30) Qin, X.; Wu, C.; Niu, D.; Qin, L.; Wang, X.; Wang, Q.; Li, Y. Peroxisome Inspired Hybrid Enzyme Nanogels for Chemodynamic and Photodynamic Therapy. *Nat. Commun.* **2021**, *12* (1), 5243. https://doi.org/10.1038/s41467-021-25561-z.
(31) Park, J.; Jiang, Q.; Feng, D.; Mao, L.; Zhou, H.-C. Size-Controlled Synthesis of Porphyrinic Metal–Organic Framework and Functionalization for Targeted Photodynamic Therapy. *J. Am. Chem. Soc.* **2016**, *138* (10), 3518–3525. https://doi.org/10.1021/jacs.6b00007.
(32) Chen, Y.-Z.; Wang, Z. U.; Wang, H.; Lu, J.; Yu, S.-H.; Jiang, H.-L. Singlet Oxygen-Engaged Selective Photo-Oxidation over Pt Nanocrystals/Porphyrinic MOF: The Roles of Photothermal Effect and Pt Electronic State. *J. Am. Chem. Soc.* **2017**, *139* (5), 2035–2044. https://doi.org/10.1021/jacs.6b12074.
(33) Wang, J.; Fan, Y.; Lee, H.; Yi, C.; Cheng, C.; Zhao, X.; Yang, M. Ultrasmall Metal–Organic Framework Zn-MOF-74 Nanodots: Size-Controlled Synthesis and Application for Highly Selective Colorimetric Sensing of Iron(III) in Aqueous Solution. *ACS Appl. Nano Mater.* **2018**, *1* (7), 3747–3753. https://doi.org/10.1021/acsanm.8b01083.
(34) Cheng, C.; Zhang, R.; Wang, J.; Zhang, Y.; Wen, C.; Tan, Y.; Yang, M. An Ultrasensitive and Selective Fluorescent Nanosensor Based on Porphyrinic Metal–Organic Framework Nanoparticles for Cu2+ Detection. *Analyst* **2020**, *145* (3), 797–804. https://doi.org/10.1039/C9AN02231G.
(35) Blouw, B.; Song, H.; Tihan, T.; Bosze, J.; Ferrara, N.; Gerber, H.-P.; Johnson, R. S.; Bergers, G. The Hypoxic Response of Tumors Is Dependent on Their Microenvironment. *Cancer Cell* **2003**, *4* (2), 133–146. https://doi.org/10.1016/S1535-6108(03)00194-6.
(36) Jiang, L.; Bai, H.; Liu, L.; Lv, F.; Ren, X.; Wang, S. Luminescent, Oxygen-Supplying, Hemoglobin-Linked Conjugated Polymer Nanoparticles for Photodynamic Therapy. *Angew. Chem. Int. Ed.* **2019**, *58* (31), 10660–10665. https://doi.org/10.1002/anie.201905884.
(37) Hu, X.; Li, J.; Chen, Y.; Long, Q.; Bai, Y.; Li, R.; Wang, K.; Jiang, M.; Chen, C.; Mao, J.; Zheng, Y.; Gao, Z. A Self-Assembly ICG Nanoparticle Potentiating Targeted

Photothermal and Photodynamic Therapy in NSCLC. *ACS Biomater. Sci. Eng.* **2022**, *8* (10), 4535–4546. https://doi.org/10.1021/acsbiomaterials.2c00620.
(38) Zhang, P.; Ouyang, Y.; Sohn, Y. S.; Fadeev, M.; Karmi, O.; Nechushtai, R.; Stein, I.; Pikarsky, E.; Willner, I. MiRNA-Guided Imaging and Photodynamic Therapy Treatment of Cancer Cells Using Zn(II)-Protoporphyrin IX-Loaded Metal–Organic Framework Nanoparticles. *ACS Nano* **2022**, *16* (2), 1791–1801. https://doi.org/10.1021/acsnano.1c04681.
(39) Li, Z.-H.; Chen, Y.; Sun, Y.; Zhang, X.-Z. Platinum-Doped Prussian Blue Nanozymes for Multiwavelength Bioimaging Guided Photothermal Therapy of Tumor and Anti-Inflammation. *ACS Nano* **2021**, *15* (3), 5189–5200. https://doi.org/10.1021/acsnano.0c10388.
(40) Xu, X.; Saw, P. E.; Tao, W.; Li, Y.; Ji, X.; Bhasin, S.; Liu, Y.; Ayyash, D.; Rasmussen, J.; Huo, M.; Shi, J.; Farokhzad, O. C. ROS-Responsive Polyprodrug Nanoparticles for Triggered Drug Delivery and Effective Cancer Therapy. *Adv. Mater.* **2017**, *29* (33), 1700141. https://doi.org/10.1002/adma.201700141.
(41) Kulkarni, P.; Haldar, M. K.; Katti, P.; Dawes, C.; You, S.; Choi, Y.; Mallik, S. Hypoxia Responsive, Tumor Penetrating Lipid Nanoparticles for Delivery of Chemotherapeutics to Pancreatic Cancer Cell Spheroids. *Bioconjug. Chem.* **2016**, *27* (8), 1830–1838. https://doi.org/10.1021/acs.bioconjchem.6b00241.